J. Fluid Mech. (2024), *vol*. 985, A8, doi:10.1017/jfm.2024.286

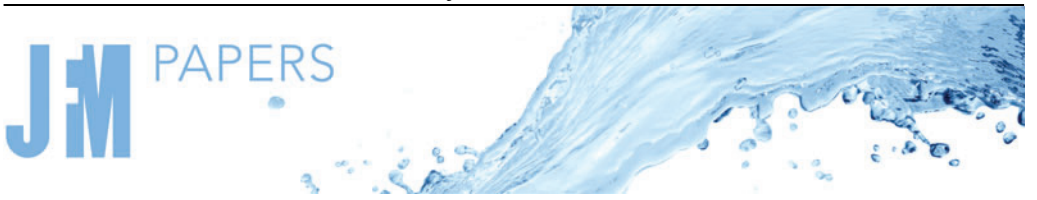

Mechanism for axial pattern formation of concentrated suspension in a horizontal rotating cylinder

Sudarshan Konidena[1,2], Bernhard Vowinckel[1], Ryohei Seto[3,4], K. Anki Reddy[5] and Anugrah Singh[2,†]

[1]Institute of Urban and Industrial Water Management, Technische Universität Dresden, 01069 Dresden, Germany

[2]Department of Chemical Engineering, Indian Institute of Technology Guwahati, 781039, India

[3]Wenzhou Key Laboratory of Biomaterials and Engineering, Wenzhou Institute, University of Chinese Academy of Sciences, Wenzhou, Zhejiang 325000, PR China

[4]Oujiang Laboratory (Zhejiang Lab for Regenerative Medicine, Vision and Brain Health), Wenzhou, Zhejiang 325000, PR China

[5]Department of Chemical Engineering, Indian Institute of Technology Tirupati, 517619, India

(Received 18 September 2023; revised 13 March 2024; accepted 13 March 2024)

We have performed numerical simulations to investigate the phenomenon of axial pattern formation exhibited by a non-neutrally buoyant concentrated suspension. Continuum modelling of the concentrated suspension is done using the suspension balance model to identify the underlying mechanism of the phenomenon. We demonstrate that axial concentration variations become amplified to axial bands owing to the influence of the second normal stress difference (N_2), and the first normal difference (N_1) accentuates the effect of N_2. We demonstrate that the end walls of the rotating cylinder are necessary to prevent the smearing out of axial bands but are not a direct cause of the phenomenon.

Key words: suspensions, particle/fluid flow

1. Introduction

Particle-laden flow in horizontal rotating cylinders is encountered in several applications, including coating processes, pharmaceutical industries, paste preparation for composite membranes, microbiological cultures, etc. This has been of interest to physicists owing

† Email address for correspondence: anugrah@iitg.ernet.in

to the several non-equilibrium phases exhibited by such systems besides the intriguing phenomenon of axial pattern formation. It is well known that heterogeneous mixtures of dry granular materials segregate under various flow conditions such as vibration, shaking, rotation and mechanical agitation (Ottino & Khakhar 2000). When a horizontal cylinder partially filled with a heterogeneous mixture of dry grains is rotated, the grains segregate by size and/or density to form axial patterns (Seiden, Lipson & Franklin 2004). The dynamic angle of repose is considered to be the control parameter for axial pattern formation for dry heterogeneous granular mixtures (Inagaki & Yoshikawa 2010). It is noted that the end walls of the rotating drum initiate axial band formation via an axial flow due to friction at the end walls (Chen, Ottino & Lueptow 2010; Arntz *et al.* 2013; Jain, Fabien & van Wachem 2023).

A rotating suspension of neutrally buoyant particles partially filling a rotating cylinder also displays axial pattern formation even with monodispersed particles (Tirumkudulu, Tripathi & Acrivos 1999; Tirumkudulu, Mileo & Acrivos 2000; Thomas *et al.* 2001; Timberlake & Morris 2002). For such cases of the rimming flow of suspensions, it has been proposed that the differential drainage of the particle and the fluid phases drives axial segregation (Timberlake & Morris 2003).

In addition, a non-neutrally buoyant dilute suspension, entirely filling a horizontal rotating cylinder, experiences axial segregation (Breu, Kruelle & Rehberg 2004; Seiden, Ungarish & Lipson 2005; Kalyankar *et al.* 2008). For dilute suspensions (volume fraction $\phi \sim 0.02$), axial variations in particle concentration are amplified by a buckling instability driving high-density regions to fall faster, subsequently drawing more particles into this region (Lee & Ladd 2005). Experimental (Kumar & Singh 2010; Nasaba & Singh 2018, 2020) and theoretical (Hou, Pan & Glowinski 2014; Lopes, Thiele & Hazel 2018; Konidena, Reddy & Singh 2019) studies indicate that the interplay between centrifugal, gravitational and drag forces causes axial bands for the dilute suspension system. However, a unifying mechanism to explain the axial pattern formation phenomenon is still lacking. The behaviour of a dense suspension in a rotating cylinder, alongside the influence of end walls, is also unexamined in previous works (Seiden *et al.* 2004). It should be emphasized that the axial banding phenomenon is not exhibited with a neutrally buoyant particle suspension fully filling a rotating cylinder; interplay between the centrifugal force, drag and gravitational force is very much essential for the axial banding phenomenon (Kalyankar *et al.* 2008; Konidena *et al.* 2018).

Understanding the mechanism of axial band formation is significant as it elucidates the (de)mixing behaviour exhibited by the viscous dense suspension. It is well known that the steady-state rheology of a non-Newtonian fluid is governed by the three degrees of freedom of the stress tensor, i.e. the viscosity (η_s) and two normal stress differences (N_1 and N_2). In concentrated suspensions, e.g. $\phi > 0.22$ (Guazzelli & Pouliquen 2018), the anisotropy of the microstructure results in the particle normal stresses which drive migration (Morris & Boulay 1999; Sierou & Brady 2002). The previous works to explore the influence of N_1, N_2 and shear-induced migration for gravity-driven particle-laden flows are sparse (Dhas & Roy 2022) and have not investigated axial patterns in rotating flows.

In this work, we perform numerical simulations by varying the three degrees of freedom of the stress tensor. The effect of the presence of cylinder end walls is also examined. We report a non-periodic axial band pattern in a rotating dense suspension resembling the discontinuous banding phase exhibited by viscous suspensions (Kalyankar *et al.* 2008; Matson, Ackerson & Tong 2008). As a significant result, we propose a mechanism for the axial pattern formation in a dense suspension, fully filling a horizontal rotating cylinder. The first two terms of the shear viscosity (η_s taken from Boyer,

Guazzelli & Pouliquen 2011) initiate an instability along the axial plane; this instability becomes accentuated by the influence of stress anisotropy. The third term of the shear viscosity (η_s given by (2.12)) $(1-\phi/\phi_m)^{-2}$, negates the action of N_2 and pushes the particle phase towards the end walls. This eventually leads to the formation of a non-uniformly distributed pattern along the axis of rotation.

2. Mathematical model and simulation set-up

To model the concentrated suspension of non-Brownian particles, we use the original version of the suspension balance model (SBM) (Nott & Brady 1994; Morris & Boulay 1999), which ascribes particle migration to gradients in the particle stress tensor $\boldsymbol{\Sigma}_p$ (Ramachandran & Leighton 2008). In the model described below, the particle stresses and the contact stresses are identical, unlike in a more generic SBM, which is a diphasic model (which has more than three degrees of freedom identified at the macroscopic level) (Lhuillier 2009; Nott, Guazzelli & Pouliquen 2011). The SBM applies the principles of conservation of mass and momentum for the fluid and particle phases. For the bulk suspension, the particle size is sufficiently large to bypass the effects of Brownian motion, and the fluid is sufficiently viscous to neglect inertia. Therefore, the steady-state mass and momentum balance equations for the conditions described are written as

$$\boldsymbol{\nabla}\cdot\boldsymbol{u}=0, \tag{2.1}$$

$$\boldsymbol{\nabla}\cdot\boldsymbol{\Sigma}+\rho\boldsymbol{g}=0, \tag{2.2}$$

where $\boldsymbol{u}$ is the velocity of the bulk suspension, $\boldsymbol{g}$ is gravity and $\boldsymbol{\Sigma}$ is the bulk suspension stress (which will be shown later in (2.7)). Using the particle volume fraction ϕ, the total mixture density ρ is given by

$$\rho=\phi\rho_p+(1-\phi)\rho_f, \tag{2.3}$$

where ρ_p and ρ_f are the densities of the particle and the fluid phases, respectively. Thus, (2.2) can be rewritten as

$$\boldsymbol{\nabla}\cdot\boldsymbol{\Sigma}+\Delta\rho\phi\boldsymbol{g}=0, \tag{2.4}$$

where $\Delta\rho\equiv\rho_p-\rho_f$. Note that the constant body force $\rho_f\boldsymbol{g}$ is omitted in (2.4).

The continuity and momentum equations ((2.1) and (2.4)) are solved in tandem with the particle-phase conservation equation given as

$$\frac{\partial\phi}{\partial t}+\boldsymbol{u}\cdot\boldsymbol{\nabla}\phi=-\boldsymbol{\nabla}\cdot\boldsymbol{j}_t, \tag{2.5}$$

with $\boldsymbol{j}_t$ being the total migration flux. Here, $\boldsymbol{j}_t$ is written as a sum of the particle migration flux due to the cross-streamline migration $\boldsymbol{j}_\perp$ and the additional flux term due to the effect of a non-neutrally buoyant particle phase $\boldsymbol{j}_g$

$$\boldsymbol{j}_t=\underbrace{\frac{2a^2}{9\eta_0}f(\phi)[\boldsymbol{\nabla}\cdot\boldsymbol{\Sigma}^p]}_{\boldsymbol{j}_\perp}+\underbrace{\frac{2a^2}{9\eta_0}f(\phi)[\Delta\rho\phi\boldsymbol{g}]}_{\boldsymbol{j}_g}. \tag{2.6}$$

In (2.6), a is the suspended particle radius and η_0 is the fluid viscosity. The parameter $f(\phi)$ is the sedimentation hindrance function, which indicates the mobility of the particle phase; its form $f(\phi)=(1-\phi/\phi_m)(1-\phi)^{\alpha-1}$ as used in this work is given by Richardson

& Zaki (1954). The parameter α is taken as 2 and the maximum volume fraction of the solid phase ϕ_m is 0.58 (Miller, Singh & Morris 2009) for the simulations in this work. Since the time evolution of migration is sufficiently slow (Breu *et al.* 2004; Kalyankar *et al.* 2008; Matson *et al.* 2008), the reported states are always near steady state

$$\boldsymbol{\Sigma} = -p\boldsymbol{I} + 2\eta_0\eta_s\boldsymbol{D} + 2\zeta_0\boldsymbol{E} + 2\zeta_3\boldsymbol{G}_3. \tag{2.7}$$

The bulk suspension stress tensor equation (2.7) is essentially decomposed in terms of its components on a tensorial basis adapted to local flow conditions. This tensorial basis is determined solely by the symmetric part of the velocity gradient, $\boldsymbol{D}$ as in Giusteri & Seto (2018). Particle stress is calculated as $\boldsymbol{\Sigma}_p = \boldsymbol{\Sigma} - \boldsymbol{\Sigma}_f$ from the knowledge of $\boldsymbol{\Sigma}_f = -p_f\boldsymbol{I} + 2\eta_0\boldsymbol{D}$. In (2.7), the terms $\boldsymbol{D}$, $\boldsymbol{E}$ and $\boldsymbol{G}_3$ for planar flows are defined in Giusteri & Seto (2018) as $\boldsymbol{D} = (\dot{\gamma}/2)[\widehat{\boldsymbol{d}}_1\widehat{\boldsymbol{d}}_1 - \widehat{\boldsymbol{d}}_2\widehat{\boldsymbol{d}}_2]$, $\boldsymbol{E} = (\dot{\gamma}/4)[-\widehat{\boldsymbol{d}}_1\widehat{\boldsymbol{d}}_1 - \widehat{\boldsymbol{d}}_2\widehat{\boldsymbol{d}}_2 + 2\widehat{\boldsymbol{d}}_3\widehat{\boldsymbol{d}}_3]$ and $\boldsymbol{G}_3 = (\dot{\gamma}/2)(\widehat{\boldsymbol{d}}_2\widehat{\boldsymbol{d}}_1 + \widehat{\boldsymbol{d}}_1\widehat{\boldsymbol{d}}_2)$. Here, $\widehat{\boldsymbol{d}}_1$, $\widehat{\boldsymbol{d}}_2$ and $\widehat{\boldsymbol{d}}_3$ are orthonormal eigenvectors of $\boldsymbol{D}$. The parametric tensor $\boldsymbol{Q}$ which captures the anisotropy of the particles in Miller *et al.* (2009) is also enveloped in (2.7). The response coefficients ζ_0 and ζ_3 are related to λ_2 and λ_3 of the parametric tensor $\boldsymbol{Q}$ in Miller *et al.* (2009) as

$$\zeta_0 = \frac{\eta_0\eta_n}{3}(1 + \lambda_2 - 2\lambda_3), \tag{2.8}$$

$$\zeta_3 = \frac{\eta_0\eta_n}{2}(1 - \lambda_2). \tag{2.9}$$

We recall that, for simple shear, one finds (Giusteri & Seto 2018)

$$N_1 = -2\dot{\gamma}\zeta_3, \tag{2.10}$$

$$N_2 = \dot{\gamma}\zeta_3 - \tfrac{3}{2}\dot{\gamma}\zeta_0. \tag{2.11}$$

Equations (2.10) and (2.11) provide a relation between the first and the second normal stress differences (N_1 and N_2, respectively) and the response coefficients (ζ_3 and ζ_0) of the constitutive relation for the bulk stress equation (2.7). The shear and normal viscosities (made dimensionless by taking the ratio with fluid viscosity η_0) are as given by Morris & Boulay (1999) and Boyer *et al.* (2011)

$$\eta_s(\phi) = \underbrace{1 + 2.5\phi\left(1 - \frac{\phi}{\phi_m}\right)^{-1}}_{\eta_{s1}(\phi)} + \underbrace{\mu^c(\phi)\left(\frac{\phi}{\phi_m - \phi}\right)^2}_{\eta_{s2}(\phi)}, \tag{2.12}$$

$$\eta_n(\phi) = \left(\frac{\phi}{\phi_m - \phi}\right)^2, \tag{2.13}$$

where $\mu^c(\phi) = \mu_1 + (\mu_2 - \mu_1)/[1 + I_0\eta_n(\phi)]$. In Boyer *et al.* (2011), it has been shown that the frictional formalism of dense suspensions can be related to their classical viscous rheology. We implement the ϕ-dependent friction law of dense suspensions proposed by Boyer *et al.* (2011) as given by (2.12). The first two terms in (2.12) are denoted as $\eta_{s1}(\phi)$, and the third term is denoted as $\eta_{s2}(\phi)$.

The simulation parameters are close to the experimental works by Kumar & Singh (2010), Kalyankar *et al.* (2008) and Matson *et al.* (2008). The length of the cylinder $L = 0.2275$ m and the diameter is $D = 0.02$ m. The average particle concentration over the surface of the cylinder is ϕ_{avg}. The size of an individual particle $D_p = 2a$, which collectively comprises the particle phase, is 200 μm, and its density $\rho_p = 1000$ kg m^{-3}.

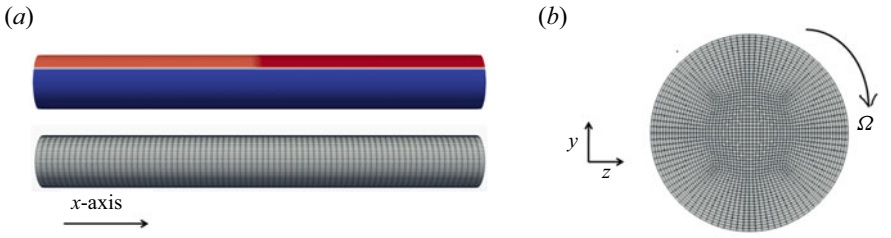

Figure 1. (*a*) Suspension concentration at $t = 0$ (concentration in the blue region is $\phi = 0.3$, dark red colour region $x \geqslant L/2$ has $\phi = 0.4625$ and light red region $x < L/2$ has $\phi = 0.4375$) and mesh along the axis of rotation. The average concentration $\phi_{avg} = 0.35$. (*b*) Radial view of the discretized geometry by structured mesh.

The suspending liquid has a density $\rho_f = 1200\,\mathrm{kg\,m^{-3}}$ with a viscosity of $\eta_0 = 0.055$ Pa s. The cylinder is rotated at a rotational velocity of $\Omega = 5$ rad $\mathrm{s^{-1}}$ and the particle velocity can be calculated using $u_p = 2a^2 g\Delta\rho/9\eta_0$, which is 0.0008 m $\mathrm{s^{-1}}$. The particle Reynolds number $Re_p = \rho_p D_p u_p/\eta_0$ is 0.0003. At time $t = 0$, the suspension configuration is as shown in figure 1(*a*), since the particles are buoyant, the concentration is higher at the top as indicated by the red colour ($\phi = 0.45$), and the blue colour indicates a concentration of $\phi = 0.3$. The values of $\zeta_0 = 0.233\eta_0\eta_n$ and $\zeta_3 = 0.1\eta_0\eta_n$ are used for the simulations, which are consistent with a concentrated suspension rheology (Miller *et al.* 2009; Xiong *et al.* 2024). The contact contribution is chosen similar to dry granular media ($\mu_2 = 0.7$, $\mu_1 = 0.32$ and $I = 0.005$) (Boyer *et al.* 2011).

3. Numerical implementation and validation

For the numerical implementation of the mathematical model detailed above, the mass, momentum and particle-phase conservation equations were solved with the open-source software OpenFOAM (Weller *et al.* 1998), which uses the finite volume method to solve the system of partial differential equations. To provide an initial instability in the concentration of the suspension along the axial plane, the concentration on the right half of the cylinder ($x > L/2$) is $\phi = 0.4625$, and on the left half of the cylinder ($x < L/2$) is $\phi = 0.4375$. The system of equations (2.1)–(2.5) is implemented by modifying the pimpleFoam solver to a custom solver which represents the SBM. More precisely, the PIMPLE (a combination of the Pressure implicit with splitting of operators method and Semi-Implicit Method for Pressure-Linked Equations) algorithm is implemented to iteratively solve (2.1) and (2.4), which describe the flow behaviour. Additionally, the transport equation (2.5) uses the Crank–Nicholson scheme in the discretization of $\partial\phi/\partial t$. Adjustable time stepping is done for simulations in this work, with the maximum allowable time step being restricted to 0.1. A rotating wall boundary condition is imposed on the wall of the cylinder with no slip. A zero flux condition is applied on the walls and surface of the cylinder for the suspension concentration.

The mesh is generated using the blockMesh facility in OpenFOAM, with a total of 189 600 hexahedral cells. Grid independence studies were performed by comparing the concentration variation across the axial length of the cylinder for three different grid sizes. The first grid has a size of 120 000 with 600 cells in the axial direction and 200 cells in the radial direction (grid-A), the second grid has a total of 189 600 with 150 cells in the axial direction and 1264 cells in the radial direction (grid-B) and the third grid studied has 240 000 cells with 150 in the axial and 1600 in the radial directions (grid-C). The concentration profiles of the suspension for the three grid sizes investigated are shown in

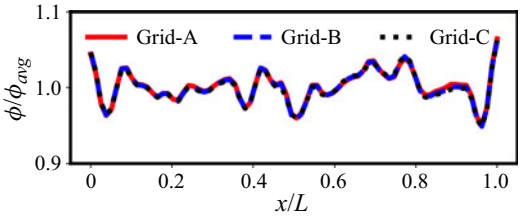

Figure 2. Grid independence studies on the rotating geometry for three different grids: grid-A with 120 000 cells, grid-B with 189 600 cells and grid-C with 240 000 cells. The concentration profiles show excellent overlap and negligible variation with different grids.

figure 2; very good agreement on the overlap of profiles indicates that the grid size has no influence on the concentration in the axial direction. For the simulations of a suspension rotating in a horizontal cylinder, we have used grid-B (189 600 cells).

In order to validate our mathematical model, we compared the concentration and velocity distributions in figures 3 and 4 for the flow of a non-neutrally buoyant suspension in a circular pipe with the MRI (magnetic resonance imaging) measurements by Altobelli, Givler & Fukushima (1991) and the numerical simulations (anisotropic and isotropic models) as discussed by Ramachandran & Leighton (2007). The concentration of the suspension compared is $\phi \sim 0.23$, radius a of the suspended particles is 0.381 mm and the cylinder radius R is given by $R = 33a$. The viscosity of suspension η is 0.384 Pa s and the densities of the suspended particles and the carrier fluid are $\rho_p = 1030$ kg m^{-3} and $\rho_f = 875$ kg m^{-3}, respectively. The study has been carried out for three different inlet velocities $u_{in} = 0.2326$ m s^{-1}, 0.07 m s^{-1} and 0.036 m s^{-1} through the conduit, which has a length of 360 cm. On the far left columns of figures 3 and 4 are the experimental results of Altobelli *et al.* (1991) and the middle columns show the numerical investigations of Ramachandran & Leighton (2007) with the left semi-circle indicating the anisotropic model and the right semi-circle representing the isotropic model. The far right columns of figures 3 and 4 contain the results generated by the mathematical model detailed in the present work.

From the experimental measurements in figures 3(*d*) and 3(*g*), it can be observed that the interface shape is concave downwards. The anisotropic models show good agreement with the concavity of the interface. The isotropic model is devoid of such a concave interface shape, as evidenced by Ramachandran & Leighton (2007) and figures 3(*e*) and 3(*h*). The present model correctly predicts the formation of a high concentration region above the tube centre, as shown by the concentration contours, however, the anisotropic model of Ramachandran & Leighton (2007) overestimates this behaviour. The only condition under which the present model displayed some disagreement in the concentration contours with the experimental measurements was at the lowest velocity, where the resuspension is under-predicted in the lower half of the conduit. In addition, it should be pointed out that there is a slight quantitative disagreement with the concentration profiles regardless of the isocontours displaying similar shapes. The concentration profile generated from the current model figure 3(*i*) shows the suspension starting to settle in the bottom half of the pipe with resuspension behaviour only near the centre of the cylinder. However, the interface shape is still in very good agreement with that from the experiments. The disagreement over the contour lines with the experimental results for $u_{in} = 0.036$ m s^{-1} could be due to a couple of reasons. First, the entrance length of the cylinder in the experiments is 117 cm, which could be insufficient to reach a fully developed state,

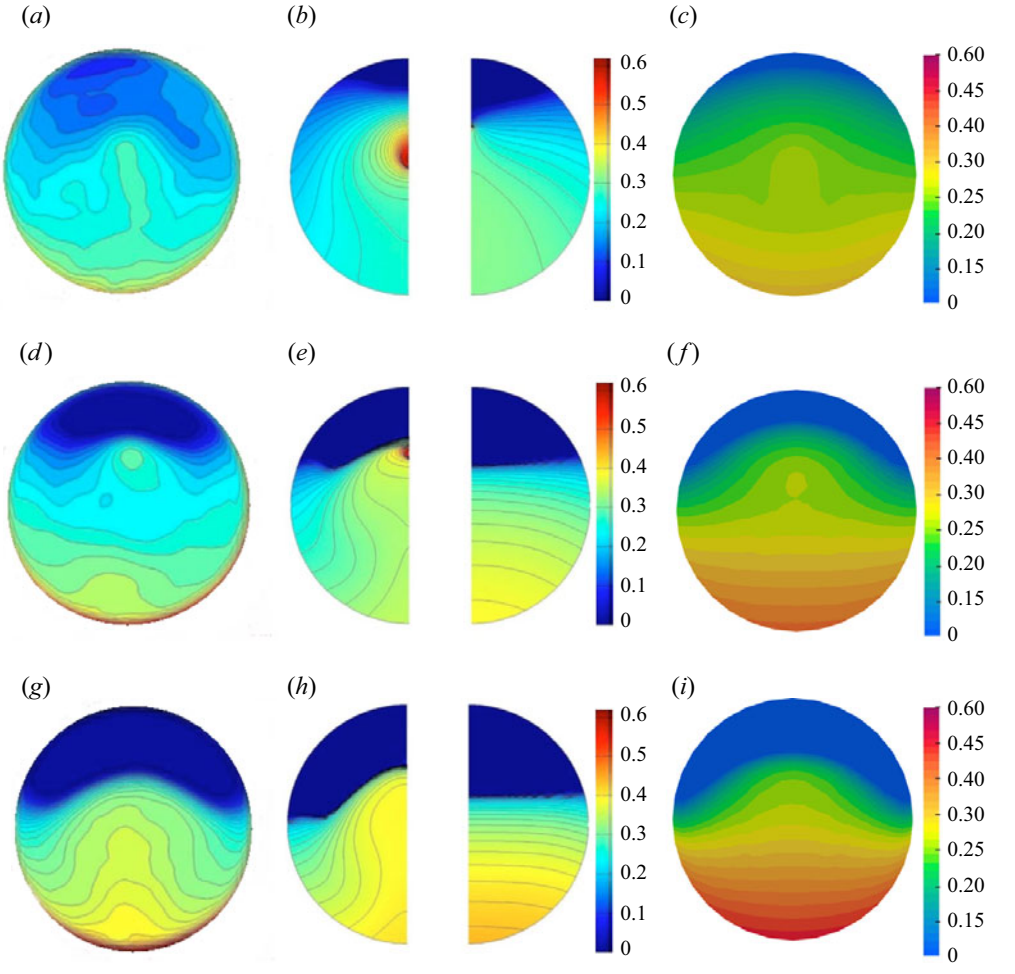

Figure 3. Comparison of concentration distribution in cylindrical channel flows with the experimental results (*a*,*d*,*g*) of Altobelli *et al.* (1991); numerical simulations (*b*,*e*,*h*) with anisotropic and isotropic models by Ramachandran & Leighton (2007); and the present SBM (*c*,*f*,*i*). Here, $u_{in} = 0.2326$ m s^{-1}, 0.07 m s^{-1} and 0.036 m s^{-1} along the rows starting from the top. First two columns are reproduced from Ramachandran & Leighton (2007), with the permission of AIP Publishing.

whereas, for the simulations performed, the pipe length is 360 cm. Second, the rheological model simply extrapolates the normal stress measurements made for $\phi \geqslant 0.3$ to $\phi \sim 0.23$ used in the experiments, which could cause deviations in the values of the observed parameters. In figure 4, we can see the comparison of the velocity data for experiments (Altobelli *et al.* 1991), anisotropic and isotropic models from Ramachandran & Leighton (2007) and the current SBM. It can be observed that the current model shows almost perfect agreement with experiments. The isotropic model overestimates the magnitude of velocity for all three inlet velocities.

The two anisotropic models, i.e. Ramachandran & Leighton (2007) and current SBM, show no such deviations in the velocity distribution. It can be concluded here that the mathematical model detailed in the previous section captures well the experimental behaviour of resuspension in pipe flow.

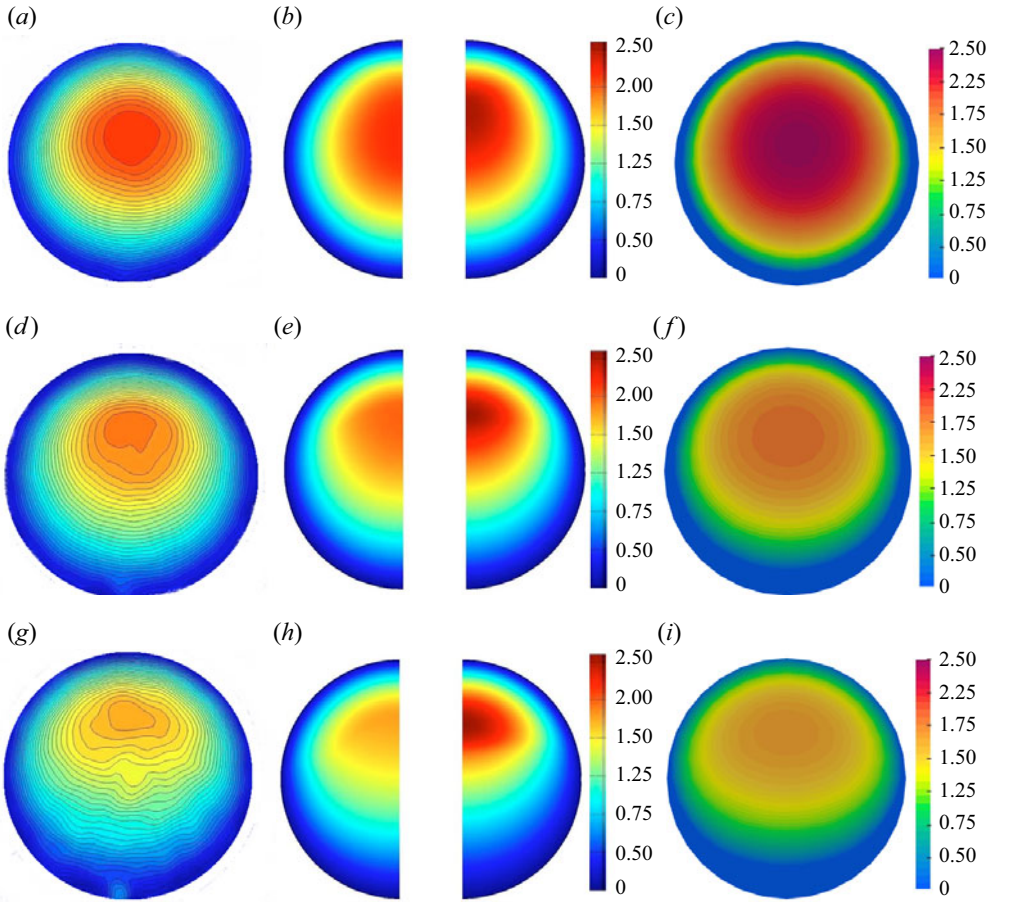

Figure 4. Comparison of velocity distribution with the experimental results (*a*,*d*,*g*) of Altobelli *et al.* (1991); numerical simulations (*b*,*e*,*h*) with anisotropic and isotropic models by Ramachandran & Leighton (2007); and the present SBM (*c*,*f*,*i*). Here, $u_{in} = 0.2326$ m s^{-1}, 0.07 m s^{-1} and 0.036 m s^{-1} along the rows starting from top. First two columns are reproduced from Ramachandran & Leighton (2007), with the permission of AIP Publishing.

4. Results and discussion

Axial pattern formation in horizontal rotating cylinders occurs in two regimes, gravitational and centrifugal force dominant (Kalyankar *et al.* 2008; Konidena *et al.* 2018). Simulations were performed in the gravitational force dominant regime to satisfy the Stokes flow condition. Since the gravitational force is dominant, axial bands are formed along the surface of the cylinder and do not extend inwards along the radial direction. The radial concentration variation becomes almost steady after 160 rotations of the cylinder, as shown in figure 5(*a*). The velocity distribution in the radial direction is shown in figure 5(*b*); it does not display any variation under rotation (for data after 40 rotations). It can also be noted that the high-concentration regions near the rotating wall are nearly two particle diameters thick. Therefore, for post-processing, the concentration of the suspension on the surface of the cylinder is extracted to investigate its variation along the length of the cylinder.

The evolution of axial bands is depicted in figure 6; the concentration fluctuations in the axial direction at around 40 rotations of the cylinder are reported. The amplitude of

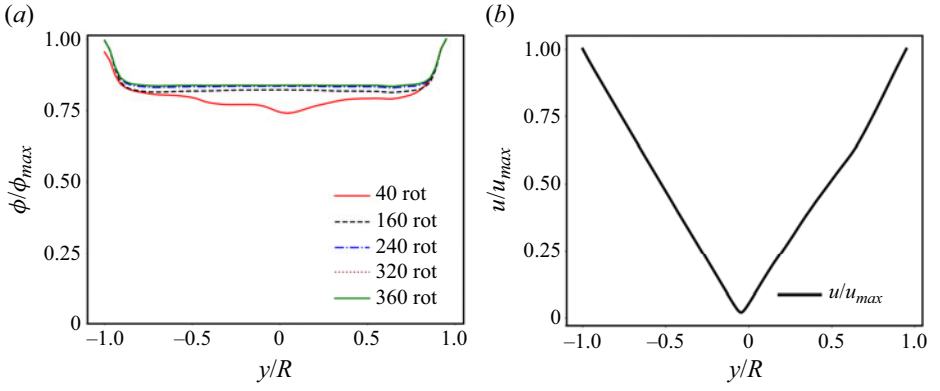

Figure 5. Concentration and velocity distributions as a function of y/R for $z = 0$ plane under rotation are shown in (a,b), respectively; (a) ϕ/ϕ_{max} vs y/R, (b) u/u_{max} vs y/R.

this axial perturbation is feeble ($\simeq 0.01\phi/\phi_{avg}$) at 40 rotations but grows for 160 rotations ($\simeq 0.04\phi/\phi_{avg}$) of the cylinder, as shown in figure 6. Axial bands start to appear near the end walls of the cylinder at 40 rotations and continue to grow until a steady state is reached at around 320 rotations of the cylinder. The axial undulation in concentration, which appears at 160 rotations of the cylinder, grows into axial concentration bands by 320 rotations. Figure 6 also suggests that the axial bands have a maximum amplitude of $\simeq 0.1\phi/\phi_{avg}$ near the end walls. Axial bands far from the end walls display an amplitude of $\simeq 0.07\phi/\phi_{\text{avg}}$ when a steady state is reached at 320 rotations of the cylinder. The non-periodic nature of the axial bands observed here is similar to the discontinuous band phase exhibited in the experiments with viscous fluids as in Kalyankar *et al.* (2008) and Matson *et al.* (2008). The location of each band remained the same even after 368 rotations of the cylinder when the simulation ended. The formation of these bands could be a consequence of either normal stress differences (NSDs) N_1 and N_2, which are reflected in (2.7) as ζ_0 and ζ_3 or η_s, which constitutes of η_{s1} and η_{s2} as encapsulated in (2.12).

The choice of equations, i.e. the constitutive relation for the total stress equation (2.7) and the relation for the shear viscosity equation (2.12), enables the isolation of NSDs (manipulation of ζ_0 and ζ_3), η_{s1} and η_{s2}. It is to be noted that, albeit not being plausible via experiments, analysing the roles of NSDs η_{s1} and η_{s2} individually allows us to determine the mechanism of axial band formation. Altering the parameters ζ_0 and ζ_3 varies the influence of the NSDs, additionally (2.12) is dissected as η_{s1} and η_{s2} to explore their respective influences on axial band formation. In other words, the mathematical model described in § 2 (denoted by $\eta_s \oplus N_1 \oplus N_2$ in the proceeding discussion), which produces axial bands as observed in Kalyankar *et al.* (2008), is tweaked to identify the underlying mechanism of the axial band formation.

To this end, the suspension stress is first nullified; this makes the suspension equivalent to a viscous Newtonian fluid as (2.12) is modified to $\eta_s = 1$. There is no undulation of concentration axially, as depicted by the red horizontal line in figure 7(a). This explains that attributes of non-Newtonian characteristics to η_s are a prerequisite for concentration disturbances along the axial plane. Second, η_{s1} is isolated; here, (2.12) becomes $\eta_s(\phi) = \eta_{s1}(\phi)$ and the parameters $\zeta_0 = 0$ and $\zeta_3 = 0$. In this case, (2.7) is devoid of NSDs and η_{s2}. The advent of axial fluctuations having an amplitude greater than $0.03\phi/\phi_{avg}$ is shown in figure 7(a) by the blue dashed line labelled η_{s1}. This observation implies that η_{s1} initiates axial undulations in the concentration in the presence of end walls. However, these

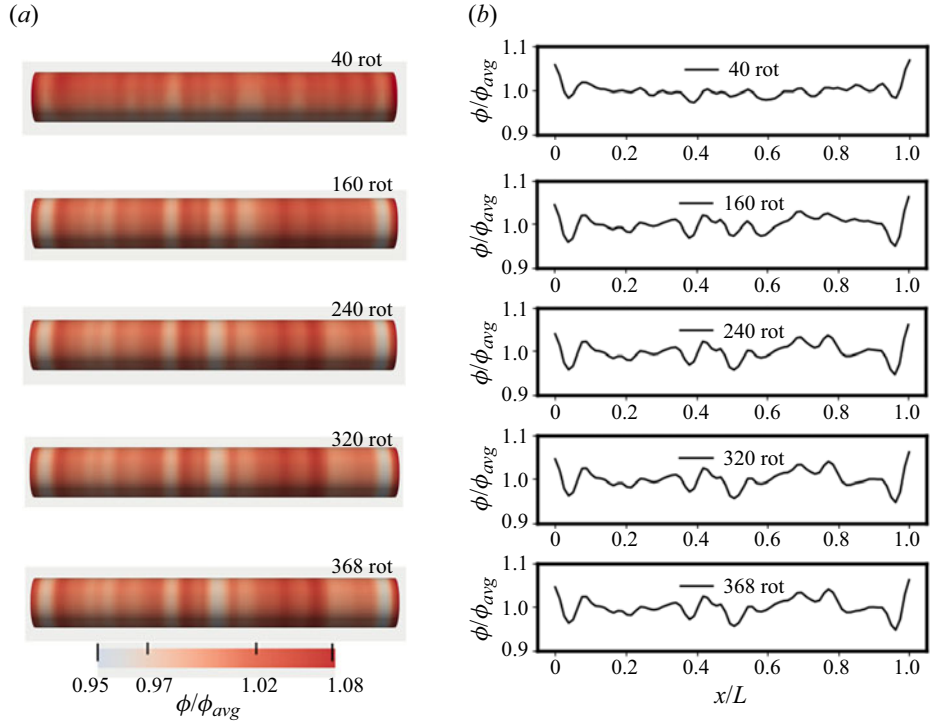

Figure 6. (*a*) Evolution of the axial band phenomenon with time for a concentrated suspension as the cylinder rotates at $\Omega = 5$ rad s^{-1}. (*b*) Evolution of the ratio ϕ/ϕ_{avg} with x/L, ϕ_{avg} being the surface average of concentration. The axial band formation is non-uniform along the axial plane at a steady state.

fluctuations with just η_{s1} (blue dashed line) in figure 7(*a*) have smaller amplitude compared with $\eta_s \oplus N_1 \oplus N_2$ (as indicated by the solid black line) at 368 rotations in figure 6(*b*), which have an amplitude of $\simeq 0.07\phi/\phi_{avg}$. As the third case; we have (2.12) as $\eta_s(\phi) = \eta_{s1}(\phi)$ with the parameters $\zeta_0 = 0.233\eta_s\eta_n$ and $\zeta_3 = 0.1\eta_0\eta_n$. This scenario represents η_{s1} with NSDs (both N_1 and N_2) incorporated, denoted by $\eta_{s1} \oplus N_1 \oplus N_2$. The concentration shows pronounced axial fluctuations, which appear almost evenly distributed, (dashed black line) in figure 6(*b*). These axial bands exhibit an amplitude $\simeq 0.09\phi/\phi_{avg}$, the highest amongst all cases investigated in this work. Consequently, it can be deduced here that η_{s1} is responsible for initiating mild undulations to the concentration in the axial plane, and NSD accentuates these undulations uniformly along the cylinder. The results also suggest that η_{s2} appears to dampen the segregation produced by the effect of NSD to form non-uniform axial bands.

We proceed to identify the roles of N_1 and N_2 exclusively on the axial banding phenomenon. Figure 8 shows the comparison of axial fluctuations when N_1 and N_2 act alongside η_{s1} ($\eta_{s1} \oplus N_1$ and $\eta_{s1} \oplus N_2$) and then in synergy with η_s ($\eta_s \oplus N_1$ and $\eta_s \oplus N_2$). For this, primarily, (2.12) is $\eta_s = \eta_{s1}$ and (2.7) has $\zeta_0 = 0$ to make $N_2 = 0$ as represented by $\eta_{s1} \oplus N_1$ (solid red line) in figure 8(*a*). The presence of N_1 is a signature of elastic effects (Seto & Giusteri 2018), with a geometrical interpretation that the eigenvectors of the stress tensor are displaced by a certain angle in the flow plane (Giusteri & Seto 2018). Synthesis of η_{s1} and N_1 produces slight axial undulations of amplitude comparable to those produced by the action of η_{s1} alone (blue dashed line in figure 7*a*). This result signifies that elastic effects due to N_1, as such, have little influence on axial pattern formation.

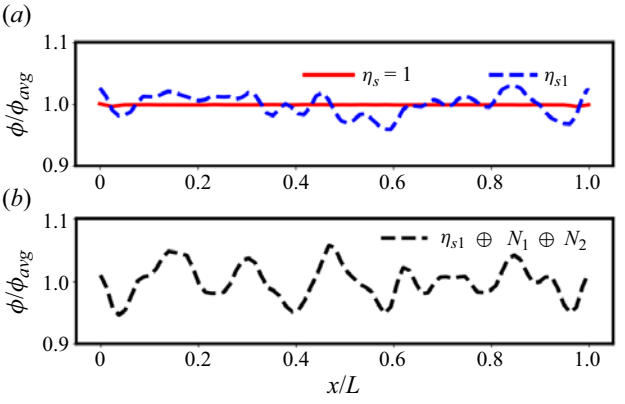

Figure 7. Axial variation in concentration at 368 rotations of the cylinder: (*a*) $\eta_s = 1$ (solid red line) and $\eta_s = \eta_{s1}$ (indicated by blue dashed line), (*b*) $\eta_s = \eta_{s1}$, $\zeta_0 = 0.233\eta_s\eta_n$, $\zeta_3 = 0.1\eta_0\eta_n$.

Second, we have $\zeta_3 = 0$ in (2.7) so that $N_1 = 0$ and $\eta_s = \eta_{s1}$; N_2 indicates tension along the vortex lines in the cross-sectional plane (Maklad & Poole 2021) and anisotropy of the normal stress originating from the planarity of the flow (Seto & Giusteri 2018). On comparing figure 8(*b*) ($\eta_{s1} \oplus N_2$) with figure 8(*a*), we can observe that the amplitude of axial fluctuations for N_2 is higher than for N_1. Moreover, it can also be deduced from figure 7(*b*) that the course of axial patterns driven by N_2 is enhanced by the action of N_1 as the axial bands have maximum amplitude when both N_1 and N_2 are in synergy ($\eta_{s1} \oplus N_1 \oplus N_2$). Finally, for the curves $\eta_s \oplus N_1$ in figure 8(*c*) and $\eta_s \oplus N_2$ in figure 8(*d*) (2.12) $\eta_s = \eta_{s1} + \eta_{s2}$, but $\zeta_0 = 0$ and $\zeta_3 = 0$, respectively. Here, it is made certain that axial bands produced by $\eta_s \oplus N_2$ are more pronounced than $\eta_s \oplus N_1$ and η_{s2} smears the concentration towards the end walls. It is also noticeable that the inclusion of η_{s2} to (2.12) only dampens the more pronounced axial banding produced by the NSD far from the end walls. This claim is consistent with the result of Carpen & Brady (2002) and Maklad & Poole (2021) that the stability of suspensions and granular flows may be affected by the presence of NSD and can be expected to enhance the intriguing behaviour of these systems.

The root mean square (r.m.s.) concentration variation over the inner portion of the cylinder (between $0.3x/L$ and $0.7x/L$) as a function of the number of rotations is depicted in figure 9. The concentration in the vicinity of the end walls is neglected in the calculation of the r.m.s. concentration variation. Figure 9 essentially emphasizes the inferences from figures 7 and 8 presented above. It can be understood from figure 9 (triangles) that $\eta_{s1} \oplus N_1 \oplus N_2$, which has the largest magnitude of concentration variation, produces the most prominent axial bands. The least growth is for $\eta_{s1} \oplus N_1$ (diamonds), which is almost equivalent to just η_{s1} (squares), as claimed in the preceding paragraph. From the above discussion following figures 7, 8 and 9, we can determine the mechanism for axial pattern formation. The parameter η_{s1} initiates axial instabilities along the axial plane; these instabilities, in turn, trigger a stress contribution isotropic in the flow plane but globally anisotropic (N_2). Therefore, the anisotropic nature (of N_2) is the major driving force for producing bands distributed uniformly along the axis of rotation, N_1 enhances the effect of N_2. However, η_{s2} dampens the amplitude of axial bands induced by the NSD, thereby producing non-uniformly distributed axial bands.

We now turn to assess the influence of the end walls of the rotating cylinder on the axial pattern formation. A periodic boundary condition (PBC) is applied on the end walls of the

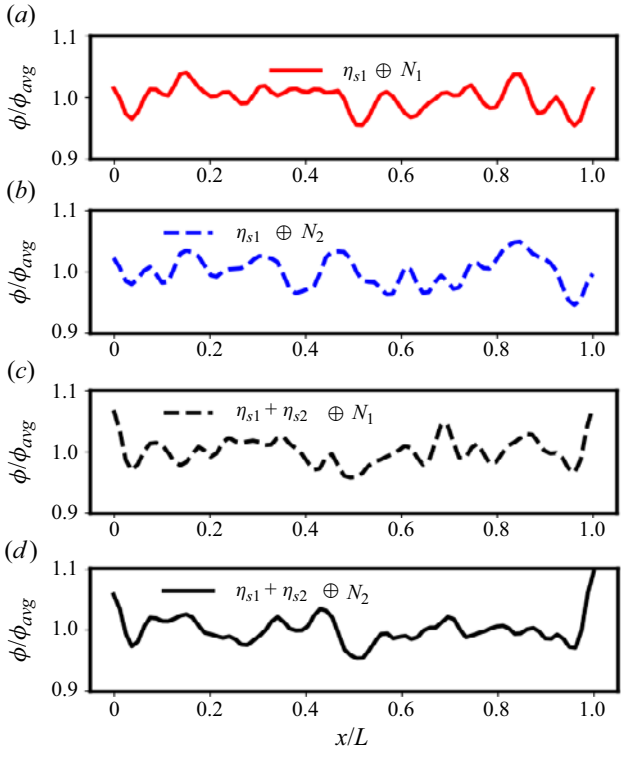

Figure 8. The influence of N_1 and N_2 in synergy with η_{s1} and η_s on axial pattern formation (at 368 rotations of the cylinder); (*a*) $\eta_s = \eta_{s1}$ and $\zeta_0 = 0$, (*b*) $\eta_s = \eta_{s1}$ and $\zeta_3 = 0$, (*c*) $\eta_s = \eta_{s1} + \eta_{s2}$ and $\zeta_0 = 0$ and (*d*) $\eta_s = \eta_{s1} + \eta_{s2}$ and $\zeta_3 = 0$.

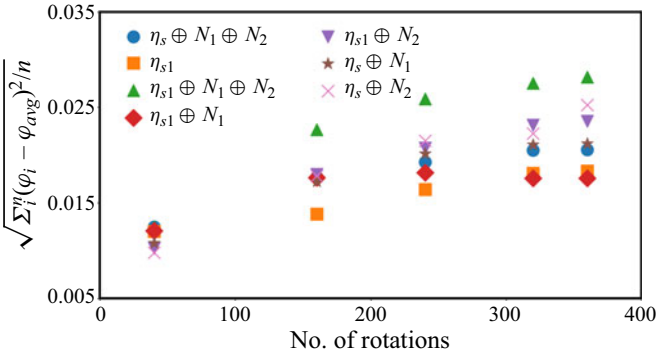

Figure 9. Comparison of r.m.s. concentration variation over the inner portion of the cylinder between $0.3x/L$ and $0.7x/L$ for various model choices investigated.

cylinder in the axial directions, breaking the problem's translational symmetry. Figure 10 depicts the concentration profile of a dense suspension at five different rotations (from 288 to 960) of the cylinder along the axial plane. It also shows that the axial fluctuations change position continuously with time, and there is no steady state as such for the system even after 960 rotations of the cylinder. The maximum amplitude of the axial fluctuations in concentration does not exceed $\simeq 0.05\phi/\phi_{avg}$ at any point during the simulations. The axial

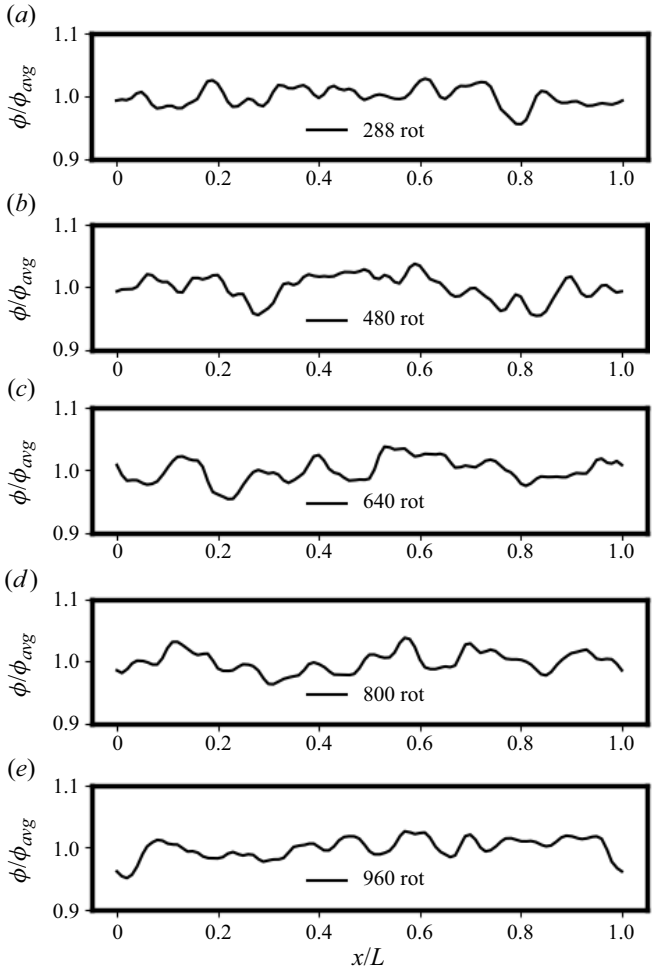

Figure 10. Evolution of concentration profiles with periodic boundary conditions along the axis of the cylinder.

fluctuations produced do not proceed to form axial bands of higher amplitude, as observed in figure 6. We have also investigated a different initial concentration distribution, where the suspension is introduced with strong axial bands of $\phi \sim 0.45$ interlaced between $\phi \sim 0.3$, and PBC applied on the end walls. The r.m.s. concentration variation along the inner portion of the cylinder (between $0.3x/L$ and $0.7x/L$) is compared in figure 11 for $\eta_s \oplus N_1 \oplus N_2$, with PBC, flat$_{init}$ (initial configuration as in figure 1) and PBC, bands$_{init}$ (with strong axial bands introduced at $t = 0$). The concentration variation in figure 11 shows an increase for PBC, flat$_{init}$ until 160 rotations before damping; however, for PBC, bands$_{init}$, the variation is continuously damped, which implies that stronger bands are not formed over time. At this point, it may be inferred that the end walls of the rotating cylinder are required to prevent the smearing of axial bands. These results demonstrate that the presence of end walls (figure 10) is essential for the formation of axial patterns but is not a cause of the banding phenomenon.

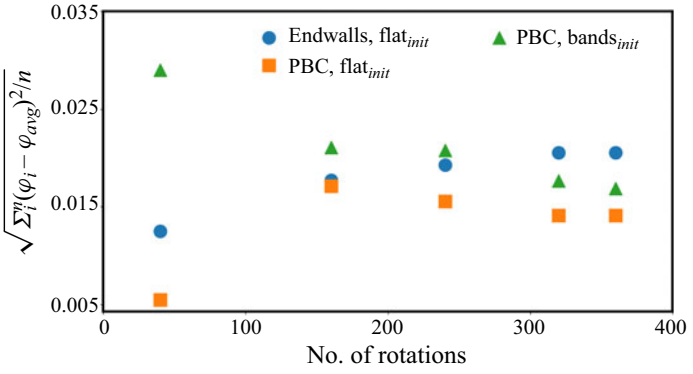

Figure 11. Comparison of r.m.s. concentration variation over the inner portion of the cylinder between $0.3x/L$ and $0.7x/L$ for '$\eta_s \oplus N_1 \oplus N_2$' (Endwalls, flat$_{init}$) and PBC with two different initial conditions, 'PBC, flat$_{init}$' as in figure 1, and 'PBC, bands$_{init}$' with uniform axial bands.

5. Conclusion

We have performed numerical simulations to identify the underlying mechanism for the axial band formation exhibited by a concentrated suspension rotating in a horizontal cylinder. The SBM, which considers the suspension as a single phase (monophasic), is used as the mathematical model. It is an analysis of how each component of the suspension rheology contributes to the axial band formation of a concentrated suspension. Axial undulations in the concentration appear to grow from as early as 40 rotations of the cylinder; these undulations develop into larger instabilities at 160 rotations and grow into axial bands as they reach a steady state at 320 rotations, as observed in figure 6.

The choice of the bulk suspension stress tensor given by (2.7) allows us to investigate the influence of NSDs on axial concentration variations via the manipulation of ζ_0 and ζ_3. In addition, the effect of the components η_{s1} and η_{s2} of suspension shear viscosity given in (2.12) on axial banding could also be probed. From the analysis of the results discussed, we propose a mechanism for the axial band formation in non-neutrally rotating suspensions. The axial bands are initiated by η_{s1}; in addition, the major driving force for the growth of these bands is the anisotropy of the suspension stress. The second NSD N_2 is primarily responsible for the demixing of the suspension in the axial plane, and the first NSD N_1 accentuates the effect of N_2 for axial banding. This is reiterated in figure 9 where the maximum r.m.s. concentration variation is shown when $\eta_s = \eta_{s1}$ is in synergy with NSD. Moreover, η_{s2} pushes the concentration towards the end walls, thereby introducing non-uniformity in the axial bands. It is noteworthy that gravity is very much essential as neutrally buoyant particle suspensions show no axial band formation, indicating an interplay between the drag, centrifugal and gravitational forces (coherent with the results of Kalyankar *et al.* 2008; Konidena *et al.* 2018). Also, a mere density mismatch between the particle phase and the carrier fluid would just produce solid-body rotation in the zero-*Re* limit with no evidence of axial band formation. Finally, the end walls of the cylinder are not a cause but are necessary to prevent the smearing of concentration from the axial bands. Apart from illustrating the (de)mixing mechanism of a monodispersed dense suspension, this study could aid in comprehending the mechanism responsible for axial and radial segregation experienced by dense binary and ternary suspensions.

Acknowledgements. S.K. is very grateful to Professor J. Morris and Professor G.G. Giusteri for their invaluable suggestions and time.

Funding. S.K. and B.V. acknowledge support through German Research Foundation (DFG) grant VO2413/3-1. R.S. acknowledges the support of the National Natural Science Foundation of China (12174390, 12150610463) and Wenzhou Institute (WIUCASQD2020002). The authors also acknowledge the Gauss Centre for Supercomputing e.V. (www.gauss-centre.eu) for providing computing time on the GCS Supercomputer SUPERMUC-NG at Leibniz Supercomputing Centre (www.lrz.de).

Declaration of interests. The authors report no conflict of interest.

Author ORCIDs.
Bernhard Vowinckel https://orcid.org/0000-0001-6853-7750;
Ryohei Seto https://orcid.org/0000-0002-4099-034X;
K. Anki Reddy https://orcid.org/0000-0002-7637-766X;
Anugrah Singh https://orcid.org/0000-0001-7980-0278.

References

Altobelli, S.A., Givler, R.C. & Fukushima, E. 1991 Velocity and concentration measurements of suspensions by nuclear magnetic resonance imaging. *J. Rheol.* **35** (5), 721–734.

Arntz, M., den Otter, W., Beeftink, H., Boom, R. & Briels, W. 2013 The influence of end walls on the segregation pattern in a horizontal rotating drum. *Granul. Matt.* **15**, 25–38.

Boyer, F., Guazzelli, É. & Pouliquen, O. 2011 Unifying suspension and granular rheology. *Phys. Rev. Lett.* **107**, 188301.

Breu, A.P.J., Kruelle, C.A. & Rehberg, I. 2004 Oscillatory patterns in a rotating aqueous suspension. *Eur. Phys. J.* E **13**, 189–196.

Carpen, I.C. & Brady, J.F. 2002 Gravitational instability in suspension flow. *J. Fluid Mech.* **472**, 201–210.

Chen, P., Ottino, J.M. & Lueptow, R.M. 2010 Onset mechanism for granular axial band formation in rotating tumblers. *Phys. Rev. Lett.* **104**, 188002.

Dhas, D.J. & Roy, A. 2022 Stability of gravity-driven particle-laden flows – roles of shear-induced migration and normal stresses. *J. Fluid Mech.* **938**, A29.

Giusteri, G.G. & Seto, R. 2018 A theoretical framework for steady-state rheometry in generic flow conditions. *J. Rheol.* **62** (3), 713–723.

Guazzelli, É. & Pouliquen, O. 2018 Rheology of dense granular suspensions. *J. Fluid Mech.* **852**, P1.

Hou, S., Pan, T.-W. & Glowinski, R. 2014 Circular band formation for incompressible viscous fluid–rigid-particle mixtures in a rotating cylinder. *Phys. Rev.* E **89**, 023013.

Inagaki, S. & Yoshikawa, K. 2010 Traveling wave of segregation in a highly filled rotating drum. *Phys. Rev. Lett.* **105** (4), 118001.

Jain, A., Fabien, E. & van Wachem, B. 2023 The effect of side walls on particles mixing in rotating drums. *Particuology* **72**, 112–121.

Kalyankar, M.G., Matson, W.R., Tong, P. & Ackerson, B.J. 2008 Pattern formation in a rotating suspension of non-Brownian buoyant particles. *Phys. Fluids* **20** (8), 083301.

Konidena, S., Lee, J., Reddy, K.A. & Singh, A. 2018 Particle dynamics and pattern formation in a rotating suspension of positively buoyant particles. *Phys. Rev. Fluids* **3**, 044301.

Konidena, S., Reddy, K.A. & Singh, A. 2019 Dynamics of bidensity particle suspensions in a horizontal rotating cylinder. *Phys. Rev.* E **99**, 013111.

Kumar, A.A. & Singh, A. 2010 Dynamics of bi-dispersed settling suspension of non-colloidal particles in rotating cylinder. *Adv. Powder Technol.* **21** (6), 641–651.

Lee, J. & Ladd, A.J.C. 2005 Axial segregation of a settling suspension in a rotating cylinder. *Phys. Rev. Lett.* **95**, 048001.

Lhuillier, D. 2009 Migration of rigid particles in non-Brownian viscous suspensions. *Phys. Fluids* **21** (2), 023302.

Lopes, A.V.B., Thiele, U. & Hazel, A.L. 2018 On the multiple solutions of coating and rimming flows on rotating cylinders. *J. Fluid Mech.* **835**, 540–574.

Maklad, O. & Poole, R.J. 2021 A review of the second normal-stress difference; its importance in various flows, measurement techniques, results for various complex fluids and theoretical predictions. *J. Non-Newtonian Fluid Mech.* **292**, 104522.

Matson, W.R., Ackerson, B.J. & Tong, P. 2008 Measured scaling properties of the transition boundaries in a rotating suspension of non-Brownian settling particles. *J. Fluid Mech.* **597**, 233–259.

Miller, R.M., Singh, J.P. & Morris, J.F. 2009 Suspension flow modeling for general geometries. *Chem. Engng Sci.* **64** (22), 4597–4610, morton Denn Festschrift.

MORRIS, J.F. & BOULAY, F. 1999 Curvilinear flows of noncolloidal suspensions: the role of normal stresses. *J. Rheol.* **43**, 1213–1237.

NASABA, J.C. & SINGH, A. 2018 Axial and radial patterns of a bidispersed suspension in a fully filled horizontal rotating cylinder. *Phys. Rev.* E **98**, 053102.

NASABA, J.C. & SINGH, A. 2020 Radial patterns and velocity field of non-Brownian suspensions in a fully filled horizontal rotating cylinder. *Adv. Powder Technol.* **31** (1), 448–463.

NOTT, P.R. & BRADY, J.F. 1994 Pressure-driven flow of suspensions: simulation and theory. *J. Fluid Mech.* **275**, 157–199.

NOTT, P.R., GUAZZELLI, E. & POULIQUEN, O. 2011 The suspension balance model revisited. *Phys. Fluids* **23** (4), 043304.

OTTINO, J.M. & KHAKHAR, D.V. 2000 Mixing and segregation of granular materials. *Annu. Rev. Fluid Mech.* **32** (1), 55–91.

RAMACHANDRAN, A. & LEIGHTON, D.T. 2008 The influence of secondary flows induced by normal stress differences on the shear-induced migration of particles in concentrated suspensions. *J. Fluid Mech.* **603**, 207–243.

RAMACHANDRAN, A. & LEIGHTON, D.T. JR. 2007 Viscous resuspension in a tube: the impact of secondary flows resulting from second normal stress differences. *Phys. Fluids* **19** (5), 053301.

RICHARDSON, J.F. & ZAKI, W.N. 1954 The sedimentation of a suspension of uniform spheres under conditions of viscous flow. *Chem. Engng Sci.* **3** (2), 65–73.

SEIDEN, G., LIPSON, S.G. & FRANKLIN, J. 2004 Oscillatory axial banding of particles suspended in a rotating fluid. *Phys. Rev.* E **69**, 015301.

SEIDEN, G., UNGARISH, M. & LIPSON, S.G. 2005 Banding of suspended particles in a rotating fluid-filled horizontal cylinder. *Phys. Rev.* E **72**, 021407.

SETO, R. & GIUSTERI, G.G. 2018 Normal stress differences in dense suspensions. *J. Fluid Mech.* **857**, 200–215.

SIEROU, A. & BRADY, J.F. 2002 Rheology and microstructure in concentrated noncolloidal suspensions. *J. Rheol.* **46**, 1031–1056.

THOMAS, P.J., RIDDELL, G.D., KOONER, S. & KING, G.P. 2001 Fine structure of granular banding in two-phase rimming flow. *Phys. Fluids* **13** (9), 2720–2723.

TIMBERLAKE, B.D. & MORRIS, J.F. 2002 Concentration band dynamics in free-surface Couette flow of a suspension. *Phys. Fluids* **14** (5), 1580–1589.

TIMBERLAKE, B.D. & MORRIS, J.F. 2003 Film depth and concentration banding in free surface couette flow of a suspension. *Phil. Trans. R. Soc. Lond.* A **361** (1806), 895–910.

TIRUMKUDULU, M., MILEO, A. & ACRIVOS, A. 2000 Particle segregation in monodisperse sheared suspensions in a partially filled rotating horizontal cylinder. *Phys. Fluids* **12** (6), 1615–1618.

TIRUMKUDULU, M., TRIPATHI, A. & ACRIVOS, A. 1999 Particle segregation in monodisperse sheared suspensions. *Phys. Fluids* **11** (3), 507–509.

WELLER, H.G., TABOR, G., JASAK, H. & FUREBY, C. 1998 A tensorial approach to computational continuum mechanics using object-oriented techniques. *Comput. Sci. Engng* **12** (6), 620–631.

XIONG, Z., ANGERMAN, P., ELLERO, M., SANDNES, B. & SETO, R. 2024 Ridge instability in dense suspensions caused by the second normal stress difference. *Phys. Fluids* **36** (2), 024111.